Article

High Photocatalytic Activity of g-C$_3$N$_4$/La-N-TiO$_2$ Composite with Nanoscale Heterojunctions for Degradation of Ciprofloxacin

Yanmin Yu [1] **, Ke Liu** [2] **, Yangyang Zhang** [1] **, Xuan Xing** [3,*] **and Hua Li** [3,*]

[1] School of Basic Medicine, Hubei University of Arts and Science, Xiangyang 441053, China; yuyanmin2005@163.com (Y.Y.); yangyangzhang2017@163.com (Y.Z.)
[2] Hubei Key Laboratory of Low Dimensional Optoelectronic Materials and Devices, Hubei University of Arts and Science, Xiangyang 441053, China; liuke@hbuas.edu.cn
[3] College of Life and Environmental Sciences, Minzu University of China, Beijing 100081, China
[*] Correspondence: xingxuanpku@163.com (X.X.); lihua@muc.edu.cn (H.L.)

Abstract: Ciprofloxacin (CIP) in natural waters has been taken as a serious pollutant because of its hazardous biological and ecotoxicological effects. Here, a 3D nanocomposite photocatalyst g-C$_3$N$_4$/La-N-TiO$_2$ (CN/La-N-TiO$_2$) was successfully synthesized by a simple and reproducible in-situ synthetic method. The obtained composite was characterized by XRD, SEM, BET, TEM, mapping, IR, and UV-vis spectra. The photocatalytic degradation of ciprofloxacin was investigated by using CN/La-N-TiO$_2$ nanocomposite. The main influential factors such as pH of the solution, initial CIP concentration, catalyst dosage, and coexisting ions were investigated in detail. The fastest degradation of CIP occurred at a pH of about 6.5, and CIP (5 mg/L starting concentration) was completely degraded in about 60 min after exposure to the simulated solar light. The removal rates were rarely affected by Na$^+$ (10 mg·L^{-1}), Ca^{2+} (10 mg·L^{-1}), Mg^{2+} (10 mg·L^{-1}), and urea (5 mg·L^{-1}), but decreased in the presence of NO$_3^-$ (10 mg·L^{-1}). The findings indicate that CN/La-N-TiO$_2$ nanocomposite is a green and promising photocatalyst for large-scale applications and would be a candidate for the removal of the emerging antibiotics present in the water environment.

Keywords: photocatalysis; ciprofloxacin; g-C$_3$N$_4$; TiO$_2$; composite material; wastewater; organic micropollutants

1. Introduction

Antibiotic pollution poses a serious threat to human health through drinking water and/or the food-chain, especially in developing countries, and how to efficiently remove it has gained great attention over the past [1–6]. Fluoroquinolones (FQs) are one of the most consumed antibiotics and have a total consumption of about 25 million kilograms every year in China [7,8]. Ciprofloxacin (CIP), as the second-generation fluoroquinolone, is extensively used in humans and animals to sterilize and fight infections due to their good oral intake and large activity spectrum [9]. Ultimately, it enters the WWTPs (wastewater treatment plants) as a result of being poorly adsorbed in the body and excreted unchanged in feces and urine [10,11]. As the quinolone ring is degraded difficultly, CIP is inefficiently removed by most wastewater and sewage treatment plants via conventional wastewater treatment technologies or is directly poured into water bodies in countries lacking effluent treatments [12]. CIP has been detected frequently in various groundwater [13], surface water [14], and seawater [15] throughout the world [12–20]. Therefore, an effective treatment technology is necessary to transform CIP into noN-Toxic, pharmaceutically less active, or more biodegradable species in order to face CIP pollution problems in water.

Semiconductor photocatalysis, which has attracted wide attention by virtue of low-cost, energy-savings, non-toxicity, and high catalytic degradation activity of organic

Int. J. Environ. Res. Public Health **2022**, *19*, 4793

2 of 17

pollutants in purifying water under solar-light irradiation, has been employed to address the problem of antibiotic wastewater and it has made great progress over the past decade [19–23]. A series of previous studies was focused on the photocatalytic degradation of CIP and the data are listed in Table 1. Gad-Allah et al. employed commercial anatase TiO_2 to degrade CIP under simulated sunlight, and the best reaction rate was obtained in natural ciprofloxacin pH (5.8) and 1000 mg/L TiO_2 [24]. Wen et al. synthesized a novel Z-scheme CeO_2–Ag/AgBr photocatalyst for photocatalytic degradation of ciprofloxacin, the degradation rate could reach 93.05% in 120 min under visible light irradiation [25]. Rahmani-Aliabadi et al. evaluated the photocatalytic activities of FeS/Fe_2S_3/zeolite by photodegradation of ciprofloxacin, and the best catalysis conditions are pH 3.7, catalyst dose of 2.8 $g·L^{-1}$, 3.8 $mg·L^{-1}$ of CIP for 102 min irradiation of the suspension [26]. Gan et al. employed different post−treatment methods to synthesize three kinds of mesoporous TiO_2 nanocrystallite aggregates and comparatively studied the removal capability of CIP by adsorption in the dark and photocatalysis under light irradiation [27]. El-Kemary et al. carried out systematic research on the photocatalytic activity of the prepared ZnO nanoparticles for the degradation of ciprofloxacin drug under UV light irradiation in aqueous solutions of different pH values [28]. Li et al. successfully prepared the magnetic 3D γ-Fe_2O_3@ZnO core-shell photocatalyst, which exhibits excellent degradation efficiency of CIP up to 92.5% under simulated sunlight irradiation [29]. Chen et al. studied the CIP decay over $Bi_2O_3/(BiO)_2CO_3$ heterojunctions under simulated solar light irradiation, where the removal efficiency achieved 93.4% in 30 min [30], and so on [16,20,29,31–41].

Table 1. Photocatalytic activity of semiconductor materials for CIP degradation under visible light irradiation.

Photocatalysts	C_0 (mg/L)	pH	Degradation Rate (%)	Light Irradiation Wavelength (λ)	Incident Light Power	Ref
Commercial anatase TiO_2	1500 ppm	5.8	Kapp = 0.02 min^{-1}	Simulated visible light	Commercial visible metal halide lamp	[24]
CeO_2–Ag/AgBr	10	-	93.05%/120 min	$\lambda > 420$ nm	A 300 W Xe lamp	[25]
FeS/Fe_2S_3/zeolite	2	-	6%/90 min	$\lambda > 380$ nm	Tungsten lamp	[26]
Mesoporous TiO_2 nanocrystallite aggregates	160	-	96.05%/6 h	200 nm ~1000 nm	A 500 W Xe lamp	[27]
ZnO	4	7/10	48%/60 min	365 nm	A xenon lamp	[28]
3D γ-Fe_2O_3@ZnO core-shell photocatalyst	10	5.8	92.5%/60 min	Simulated sunlight	A 300 W Xenon lamp	[29]
$Bi_2O_3/(BiO)_2CO_3$	10	4.0~8.3	93.4%/30 min	Simulated solar light	A 300 W Xenon lamp	[30]
Ag@PCNS/$BiVO_4$	10	-	92.6%/120 min 17.5%/120 min	$\lambda > 420$ nm $\lambda > 760$ nm	-	[31]
ZnAl-LDH/g-C_3N_4	20	-	84.1%/150 min	-	A 35 W Xenon lamp	[35]
Ag_2CrO_4/Ag/$BiFeO_3$@RGO	10	6	96%/60 min	Visible light	450 mW cm^{-2}	[33]
TiO_2 nanorod/g-C_3N_4 nanosheet	4.97	6.3	93.4%/60 min	Simulated sunlight	A 500WXenon lamp	[34]
TiO_2@g-C_3N_4 hollow	-	-	74%/120 min	Simulated sunlight	-	[32]
CN/La-N-TiO_2	10	6.0–7.0	96.8%/60 min	$\lambda > 420$ nm	A 300 W Xe lamp	our work

C_0: the initial concentration. PMS: peroxymonosulfate.

From Table 1, it is can be found that the existing research mainly focuses on simulating wastewater degradation in the laboratory and little research on the catalytic degradation of

Int. J. Environ. Res. Public Health **2022**, *19*, 4793

3 of 17

CIP by the semiconductor photocatalytic systems in different water matrices (river water, synthetic wastewater similar by composition to wastewater of pharmaceutical industry). Therefore, further optimization and innovation of the semiconductor photocatalysts for catalytic degradation of CIP in actual wastewater are still in great demand. Hence, in this work, the semiconductor photocatalysis (CN/La-N-TiO$_2$) will be applied to remove ciprofloxacin in an actual water environment.

TiO$_2$-assisted photocatalysis has attracted widespread attention to purify polluted water by the removal of organic pollutants, owing to its good stability, low-budget, non-toxicity, and excellent photocatalytic performance [42,43]. It has been demonstrated that TiO$_2$ doped with elements such as N, P, S, B, C, Co, and La, is an effective way to introduce impurity energy levels, change the intrinsic band structure, reduce the bandgap and improve the photocatalytic capability under visible light [39,41,44]. Lanthanide is a good candidate because its low-valent doping results in the formation of oxygen vacancies on the exterior or surface lattice and hence improves the catalytic activity [41,45,46]. In our previous research work, TiO$_2$ co-doped with nitrogen and lanthanum/gadolinium ([Xe]5d^{1}6s^2/[Xe]4f^{7}5d^{1}6s^2 electronic configuration) was successfully synthesized using urea and lanthanum nitrate as a precursor, and the result is that La or Gd-N codoping could significantly improve the photocatalytic activity and thermal stability of TiO$_2$ [42,47]. In addition to ion doping, the highly optically active heterojunction structures also could effectively reduce recombination of electron-hole pairs, broaden the spectral response range and enhance photocatalytic activity. g-C$_3$N$_4$ nanosheets with hybrid engineering architectures exhibit superior chemical stability and photocatalytic decomposition activity of organic pollutants under visible light due to distinct electronics and morphological behavior [22,23,34,41,48,49]. The addition of g-C$_3$N$_4$ nanosheet with La-N-TiO$_2$, as the appropriate band position of La-N-TiO$_2$ can match well with that of g-C$_3$N$_4$ to effectively hinder the recombination of photo-generated carriers, which improves the intrinsic electrical conductivity, results in a good electrochemical performance of g-C$_3$N$_4$/La-N-TiO$_2$ composites.

Hence, in this work, the composite materials, made of graphitic carbon nitride/lanthanum and nitrogen co-doped titanium dioxide (g-C$_3$N$_4$/La-N-TiO$_2$), have been successfully fabricated for the efficient photocatalytic degradation of ciprofloxacin (CIP). A 96.8% degradation of CIP was achieved in 60 min under the conditions of 0.75 g·L^{-1} CN/La-N-TiO$_2$, 10 mg·L^{-1} CIP, and pH of 6.5. It was applied to remove CIP in the collected Danjiangkou Water sample, and the degradation efficiency was close to that of laboratory simulated wastewater. The intermediates and the suggested mineralization pathway of CIP were analyzed and discussed. The findings indicate that CN/La-N-TiO$_2$ nanocomposite is a green and promising photocatalyst for large-scale applications and would be a candidate for the removal of the emerging antibiotics present in the water environment.

2. Materials and Methods

2.1. Materials

We purchased urea (CH$_4$N$_2$O), La(NO$_3$)$_3$, dicyandiamideand (99%), and TiCl$_4$ from Sinopharm Chemical Reagent Co. (Shanghai, China) Ti(OCH(CH$_3$)$_2$)$_4$ and P123 (PEO-PPO-PEO) were purchased by Sigma-Aldrich. The water used throughout all of the experiments was purified using a Millipore system.

2.2. Synthesis of g-C$_3$N$_4$/La-N-TiO$_2$ (CN/La-N-TiO$_2$) Composite Nanomaterials

g-C$_3$N$_4$ was prepared according to a reported procedure [50]. Given amounts of P123, La(NO$_3$)$_3$, and urea were mixed in 20 mL anhydrous ethanol, 0.44 mL TiCl$_4$, and 2.1 mL (CH$_3$CH$_3$CHO)$_4$Ti were added after vigorous stirring for 2 h at room temperature, then it continued to stir for 3 h. The resulting mixture was sealed in a crucible with a cover to aging for 48 h at room temperature. Before drying at 60 °C for 8 h, a certain amount of dicyandiamide (20, 30, 50, 70, or 100 mg) was added. Then, the dried samples were subjected to calcination at the temperature of 580 °C for 5 h with a heating rate of 2.0 °C·min^{-1}. Finally, g-C$_3$N$_4$/La-N-TiO$_2$(CN/La-N-TiO$_2$) powder products were obtained and ground thor-

oughly. In control experiments, the samples of different elements doped were synthesized under identical conditions, marked as La-N-TiO$_2$, CN/N-TiO$_2$, and CN/La-TiO$_2$.

2.3. Spectroscopic and Electron Microscopic Characterization

Physicochemical properties of the prepared catalyst were thoroughly characterized as follows: X-ray diffraction (XRD) patterns were recorded on XD-3 X-ray diffraction, fitted with a Cu Kα radiation (λ = 1.54 Å). Fourier transform infrared (-FTIR) spectroscopy was measured on a Bruker VERTEX 70v FTIR Spectrometer for samples embedded in KBr pellets. Surface morphologies and structure features were observed with a field emission scanning electron microscope (FE-SEM, Hitachi s-4800, Tokyo, Japan) at an accelerating voltage of 10 kV, transmission electron microscopic (TEM, FEI-Talos F200S, Hong Kong, China) at an accelerating voltage of 200 kV, and STEM mapping. UV-vis diffuse reflectance spectra (DRS) of the samples were collected on a Perkin Elmer Lambda 950 UV-vis spectrophotometer equipped with an integrating sphere attachment (BaSO$_4$ as the reference) within the range of 200–1000 nm. The elemental composition and the chemical state of the samples were confirmed by X-ray photoelectron spectroscopy (Thermo Scientific Escalab 250Xi, Waltham, MA, USA) with a Mg Kα source.

2.4. Photocatalytic Tests

The visible light photocatalytic performances of CN/La-N-TiO$_2$, CN/N-TiO$_2$, CN/La-TiO$_2$, and La-N-TiO$_2$ were evaluated by the degradation of ciprofloxacin in an aqueous solution containing a concentration of (5–20) mg/L ciprofloxacin and 0.75 g/L catalyst in 200 mL glass vessels. The suspension was stirred vigorously in dark for 30 min to achieve adsorption-desorption equilibrium between the catalysts and the ciprofloxacin, and then was irradiated under a 350 W Xe lamp light source (PLS-SXE300, Shanghai Bilang Plant, Shanghai, China) with an optical filter, λ > 420 nm. Sample was taken out periodically of the reactor, then centrifuged at 9000 rpm and analyzed by a UV-vis spectrophotometer (JASCO V-750, Tokyo, Japan). The rate of photocatalytic ciprofloxacin degradations was obtained by recording the changes in absorbance of the reaction solution. HR-MS (Thermo Scientific Q Exactive, Waltham, MA, USA) was used to analyze the byproducts formed during the photocatalytic degradation of CIP.

3. Results and Discussion

3.1. Photocatalysts Characterization

3.1.1. XRD and -FTIR Spectra

The crystal structure of the as-prepared g-C$_3$N$_4$, La-N-TiO$_2$, and CN/La-N-TiO$_2$ was characterized by XRD, and the results are shown in Figure 1a. The diffraction peaks at 2θ = 25.29°, 37.87°, 48.09°, 53.83°, 55.13°, and 62.81° in the XRD pattern of La-N-TiO$_2$/CN/La-N-TiO$_2$ correspond to (101), (004), (200), (105), (211), and (204) diffraction planes of anatase TiO$_2$ (JCPDS No. 98-4921), correspondingly [34]. The diffraction peak at 2θ = 27.0° (indexed as the (002) peak for graphitic materials) of g-C$_3$N$_4$ is attributed to the interplanar stacking of aromatic systems, which slightly shifted to 27.61° following the hybridization of La-N-TiO$_2$ and g-C$_3$N$_4$, revealing the reduction of layer spacing and the formation of denser g-C$_3$N$_4$ structures [23,51]. It is obvious that La-N-TiO$_2$ and CN/La-N-TiO$_2$ exhibit similar diffraction patterns, except for a characteristic peak at 2θ = 27.0° for CN/La-N-TiO$_2$, so it can be concluded that g-C$_3$N$_4$ was successfully decorated in the composite. The amount of dicyandiamide on the crystal structure of CN/La-N-TiO$_2$ composite was investigated (Figure S1a, Supporting Information). In Figure S1b, when the amount of dicyanide added is 70 mg, CN/La-N-TiO$_2$ composite exhibits the strongest photocatalytic activity. In this study, the optimal amount of dicyanide is 70 mg.

Int. J. Environ. Res. Public Health **2022**, *19*, 4793

5 of 17
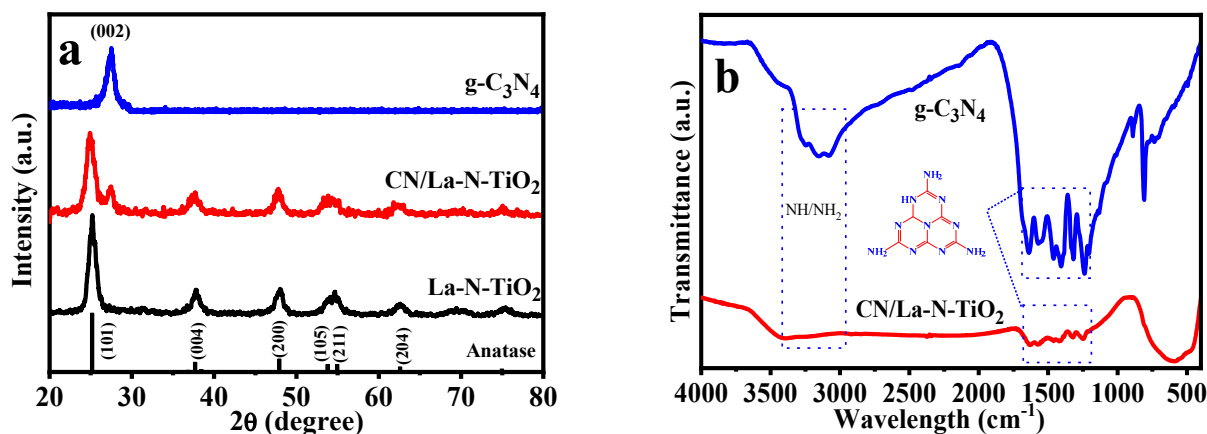
Figure 1. XRD patterns (**a**) of g-C$_3$N$_4$, La-N-TiO$_2$, and CN/La-N-TiO$_2$, and FTIR spectra (**b**) of La-N-TiO$_2$ and CN/La-N-TiO$_2$.

FTIR was used to further study the surface functional groups and chemical structures of g-C$_3$N$_4$ and CN/La-N-TiO$_2$ (Figure 1b). The vibration peaks in the range of 1200–1700 cm^{-1} are attributed to the typical CN heterocycles rings stretching [52]. The characteristic absorption band at 811 cm^{-1} could be observed, which is commonly ascribed to an s-triazine ring system [53]. The broad band adsorption peak in the range of 3150–3340 cm^{-1} corresponds to the stretching vibration modes of the terminal NH$_x$ group [54,55]. In the case of CN/La-N-TiO$_2$, in addition to the above peaks of g-C$_3$N$_4$, there are other strong absorption peaks at 500–800 cm^{-1}, which are related with the Ti-O and Ti-O-Ti bands [34].

3.1.2. Morphology Analysis

The surface morphology and structure of representative samples were examined by SEM and TEM (Figure 2). It can be found from Figure 2a that the appearance of these incompletely separated La-N-TiO$_2$ nanoparticles is spherical-like -nanoparticles with an average particle size of 10–20 nm. Figure 2b shows that the 2D-g-C$_3$N$_4$ nanosheets own curved nanosheets with lamellar morphology, and their surface is smooth and soft. As Figure 2c shows, the surface of the g-C$_3$N$_4$ nanosheet is covered by the La-N-TiO$_2$ particles to form a highly uniform composite heterojunction structure of the CN/La-N-TiO$_2$ composite. The decorated and robustly 2D-g-C$_3$N$_4$ attached with the structure of the La-N-TiO$_2$ nanoparticle to form a 3D nanocomposite photocatalyst g-C$_3$N$_4$/La-N-TiO$_2$(CN/La-N-TiO$_2$), which can provide a larger surface area, enhance the surface permeability and porous property. The TEM image provides a more evident observation of the two components in Figure 2d. The black and dark gray irregular dots located on the g-C$_3$N$_4$ nanosheet were from La-N-TiO$_2$ nanoparticles. The darker part with a spherical shape should be La-N-TiO$_2$ and the lighter part is g-C$_3$N$_4$. The size of La-N-TiO$_2$ in the CN/La-N-TiO$_2$ composite is smaller than that of the pristine La-N-TiO$_2$, which is due to the confinement of CN against the self-assembly of small component TiO$_2$ nanoparticles to a certain extent [56]. Two clearly crystal lattice fringes of 0.388 and 0.365 nm can be observed in Figure 2d. The resolved d spacing matched well with the (101) planes of TiO$_2$.

The TEM elemental mapping images of CN/La-N-TiO$_2$ are shown in Figure 3a–g, which reveal the uniform and homogenous presence of Ti, O, N, and La elements and further demonstrate that La-N-TiO$_2$ nanoparticles were evenly dispersed over the g-C$_3$N$_4$ nanosheet. It may be beneficial for the interfacial electron transfer between g-C$_3$N$_4$/La-N-TiO$_2$.

Int. J. Environ. Res. Public Health **2022**, *19*, 4793

6 of 17
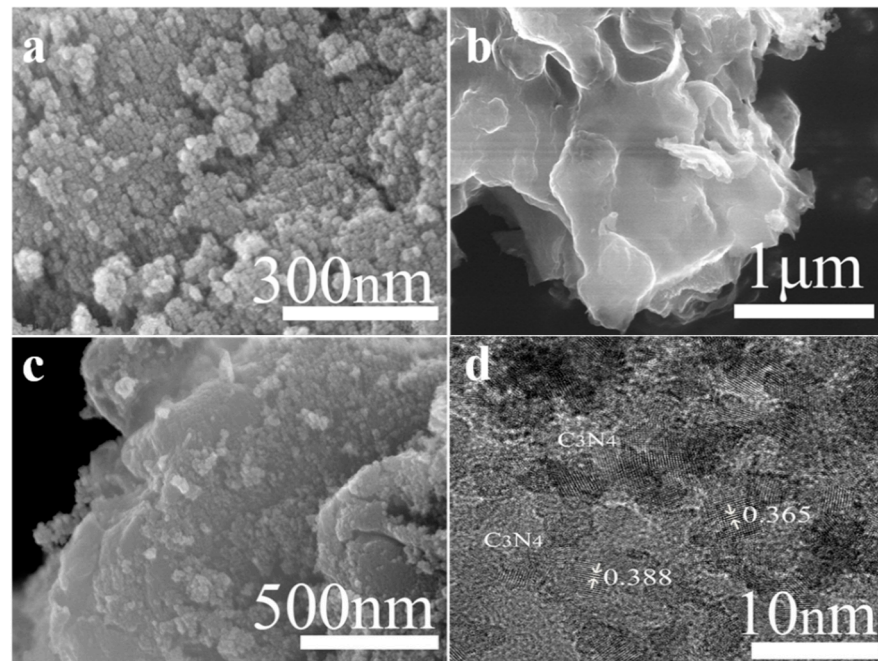
Figure 2. SEM images of La-N-TiO$_2$ (**a**), g-C$_3$N$_4$ (**b**), CN/La-N-TiO$_2$ (**c**), and TEM images of CN/La-N-TiO$_2$ (**d**).
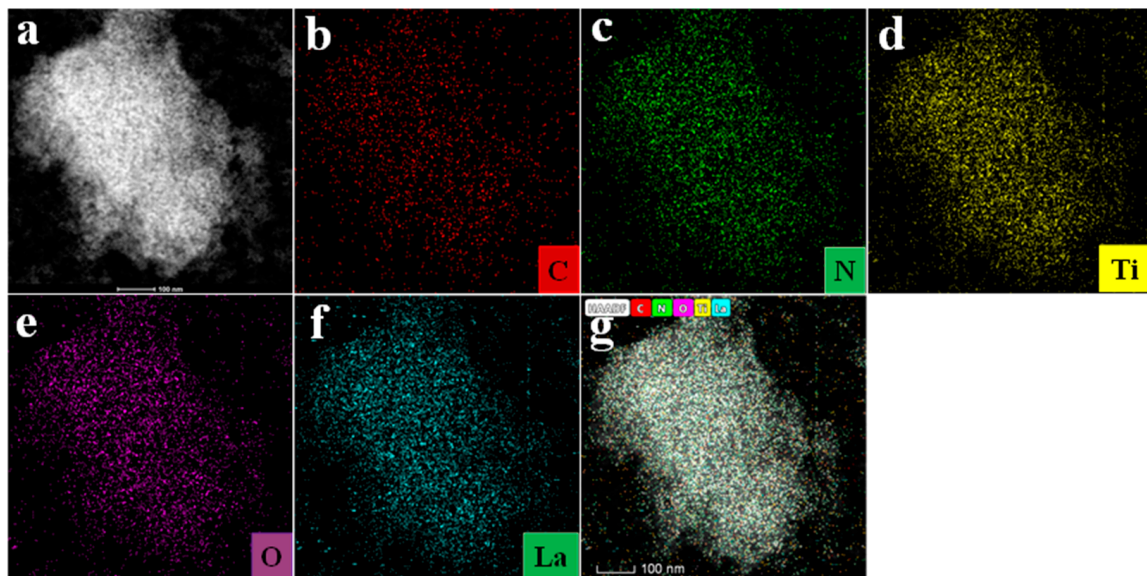
Figure 3. (**a**–**g**) TEM mapping images of CN/La-N-TiO$_2$ photocatalyst at high magnifications.

The composition and element valence of g-C$_3$N$_4$, La-N-TiO$_2$, and CN/La-N-TiO$_2$ materials were investigated by XPS measurement (Figure 4). The full survey XPS spectrum (Figure 4a) shows obvious signals of Ti 2p, O 1s, C 1s, N 1s, and La 3d, clearly indicating the existence of C, O, Ti, N, and La in CN/La-N-TiO$_2$. This result is consistent with the chemical composition, as proven by the XRD and TEM mapping.
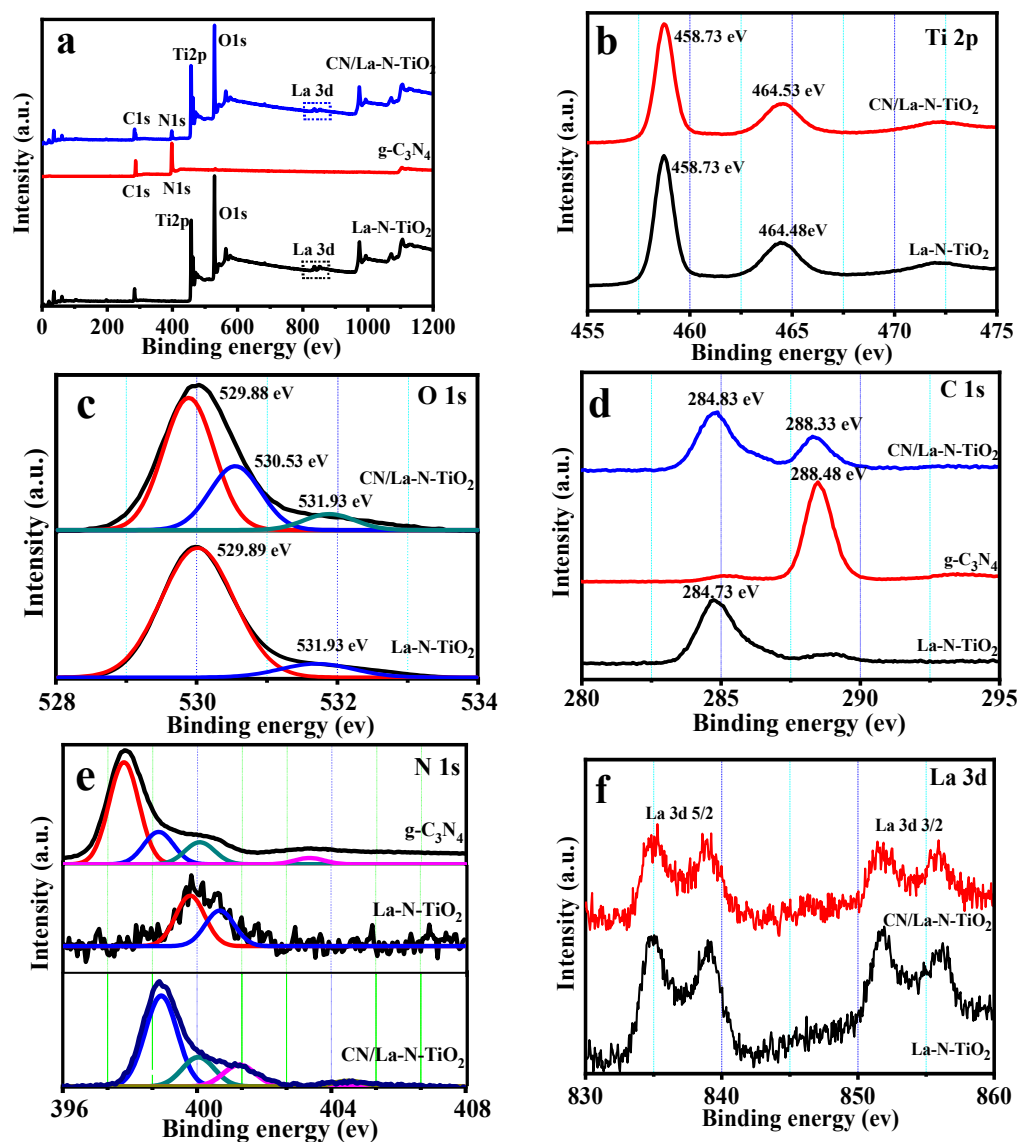
Figure 4. XPS survey spectrum (**a**); high-resolution XPS spectra of Ti 2p (**b**), O 1s (**c**), C 1s (**d**), N 1s (**e**), and La 3d (**f**).

3.1.3. XPS Analysis

As can be seen from Figure 4b, binding energy peaks at 458.7 and 464.4 eV in the high-resolution Ti 2p spectrum are assigned to Ti $2p_{3/2}$ and Ti $2p_{1/2}$, respectively, revealing the characteristic value of Ti(IV) oxidation state in TiO_2 [42]. Compared with La-N-TiO_2, there is little change in Ti 2p peaks for the CN/La-N-TiO_2.

The high-resolution O 1s XPS spectrum (Figure 4c) of La-N-TiO_2 is fitted with two peaks centered at 529.89 and 531.93 eV, which correspond to Ti-O-Ti and O-H species, respectively. Three fitted peaks located around 529.88, 530.53, and 531.93 eV in the high-resolution O 1s spectrum of CN/La-N-TiO_2 correspond to Ti-O-Ti, O-H species, and adsorbed molecular oxygen groups, respectively [39]. There is a positive shift of O 1s peaks for the CN/La-N-TiO_2 (from 529.88 to 529.89 eV). This shift is a consequence of the interaction between La-N-TiO_2 and g-C_3N_4 in heterojunctions to increase the effective positive charge on the O species [27].

There are mainly two carbon species presented in the C1s spectra (Figure 4d), which are ascribed to the C-C and/or adventitious carbon at 284.83 eV and sp^2-bonded carbon atom in the N-C=N group at 288.33 eV, respectively [23]. The sp^2-bonded carbon atom is considered the major carbon in g-C_3N_4.

The N 1s spectra of g-C_3N_4 could be fitted into three peaks (sp^2-hybridized N involved in triazine rings (C-N=C) at 396.70 eV, tertiary N group (N-(C)$_3$) at 398.70 eV and uncondensed amino group (-NH$_x$) in the aromatic skeleton at 400.30 eV), indicating the presence of sp^2-bonded graphitic carbon nitride (g-C_3N_4). The weak peak signal at 403.4 eV is attributed to the charge effect or positive charge localization of the heterocycles. The basic substructure units of g-C_3N_4 polymers [55]. There are two peaks in the XPS spectrum of N1s at 399.70 eV and 400.60 eV for La-N-TiO_2, which suggest two coexisting chemical states of the N in doped TiO_2 substitution doping (N-Ti–O) and N existed in the TiO_2 lattice (Ti–O–N–O) [43]. The N 1s spectra of CN/La-N-TiO_2 could be deconvoluted into four peaks at 398.5 eV, 398.8 eV, 400.1 eV, and 401.3 eV, respectively, corresponding to sp^2-hybridized N (C-N=C), tertiary N group (N-(C)$_3$), uncondensed amino group (-NH$_x$), and substitution doping nitrogen (N-Ti–O). Compared with g-C_3N_4 and La-N-TiO_2, there is an obvious binding energy shift of the N 1speaks in CN/La-N-TiO_2, indicating that strong interaction exists between g-C_3N_4 and La-N-TiO_2 [42,54].

According to the XPS investigation (as shown in Figure 4f), there are four peaks located at (834.8 eV, 838.40 eV) and (852.35 eV, 855.54 eV), which are attributed to La 3d$_{5/2}$ and La 3d$_{3/2}$, respectively, confirming that La^{3+} has been successfully doped into CN/La-N-TiO_2 samples. As the radius of La^{3+}(1.03 Å) is larger than the radius of Ti^{4+} (0.745 Å), La^{3+} can only form the La-O-Ti bond on the surface, and the La-O-La bond on the interstitial site of TiO_2 lattice, instead of entering into the bulk lattice of TiO_2 [41,57].

The atomic ratios of the relative elements, calculated from the XPS spectra, are summarized in Table 2. The C/N ratios for all cases of heating dicyandiamide are lower than 0.75 for the ideal crystal g-C_3N_4 [23,51–53,55]. From Table 2, the g-C_3N_4 nanosheet in this work is the ideal crystal. Combining the experimental results of XRD, SEM, TEM, and XPS, it can be concluded that the chemical combination existed on the interface between La-N-TiO_2 and g-C_3N_4 nanosheet.

Table 2. Atom concentrations, specific surface area (S$_{BET}$), pore size, and band gap of the synthesized samples.

| Catalysts	C$_1$/at.%	C$_2$/at.%	Ti/at.%	O/at.%	N/at.%	La/at.%	Surface Area (m^2/g)	Av Pore Size (nm)	Pore Volume (cm^3/g)
La-N-TiO_2	15.71	–	19.51	51.62	1.55	0.6	83 [47]	5.10	0.17
g-C_3N_4	–	31.298	–	–	66.789	–	50 [42]	–	–
CN/La-N-TiO_2	12.64	6.94	19.15	48.69	12.52	0.06	122	8.76	0.28

3.1.4. BET Surface Area Analysis

In Figure 5a, the N_2 adsorption/desorption isotherm of CN/La-N-TiO_2 shows a typical type IV curve with an H1-type hysteresis loop according to IUPAC classification, confirming the presence of mesopores [42]. Two peaks are observed from the pore distribution curve (Figure 5b), one at 4 nm is attributable to the confined self-assembled La-N-TiO_2 component nanoparticles, and the other broad peak centering at 50 nm is probably formed from gaps between CN nanosheets and La-N-TiO_2, caused by the steric confinement of crumpled and entangled nanosheet structure of seeded CN against La-N-TiO_2 growth [56]. The data of S$_{BET}$, total pore volume, and average pore diameter of La-N-TiO_2, g-C_3N_4, and CN/La-N-TiO_2 are summarized in Table 2. Compared with g-C_3N_4 (50 m^2·g^{-1}) and La-N-TiO_2 (83 m^2·g^{-1}), CN/La-N-TiO_2 possesses the highest surface area of ~122 m^2·g^{-1} and larger pore size of ~8.76 nm and the total pore volume of 0.28 cm^3·g^{-1}. The higher specific surface areas of the as−prepared hybrids benefit the penetration and adsorption of pollutants on the surface of photocatalysts, which may result in a quick transport of reaction species onto the active sites.

Int. J. Environ. Res. Public Health **2022**, *19*, 4793

9 of 17
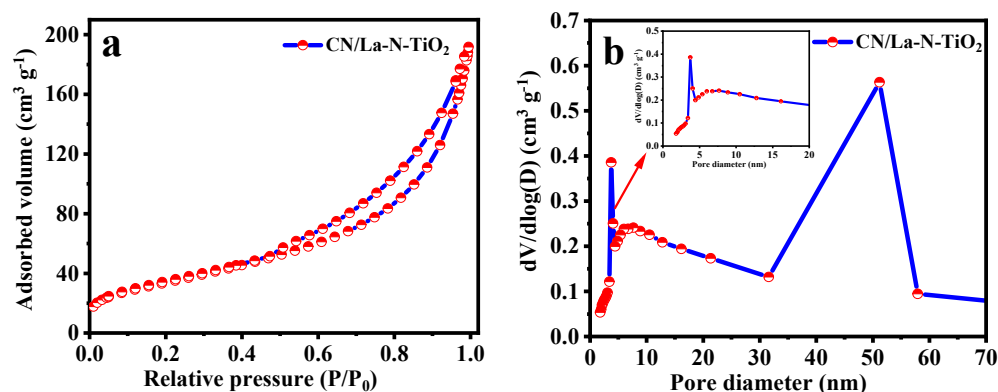
Figure 5. (**a**) N_2 adsorption−−desorption isotherms and (**b**) the corresponding pore size distribution plots of CN/La-N-TiO$_2$.

3.1.5. Spectral Properties

The characteristic light absorption spectra of the catalysts are presented in Figure 6a. The absorption edges of La-N-TiO$_2$ and g-C$_3$N$_4$ are 400 nm and 475 nm, respectively. The absorption edges of CN/La-TiO$_2$ and CN/La-N-TiO$_2$ redshift to 525 nm and 550 nm. In addition, their light absorption intensities further increased compared with g-C$_3$N$_4$ and La-N-TiO$_2$, which indicates the broadened light absorption range and the enhanced light-harvesting capacity of CN/La-TiO$_2$ and CN/La-N-TiO$_2$. Compared with g-C$_3$N$_4$, CN/N-TiO$_2$ shows a weakened light absorption intensity and a narrowed light absorption range, which may be due to the additional amount of g-C$_3$N$_4$. The bandgap energy (E$_g$) is the important parameter for predicting photophysical and photochemical properties of semiconductors [42,58]. The E$_g$ is determined by using the relationship between $(\alpha h\upsilon)^{1/2}$ and photon energy and obtained through the linear extrapolation of the intercepts on the x axis (Figure 6b). The E$_g$ of g-C$_3$N$_4$, La-N-TiO$_2$, CN/N-TiO$_2$, CN/La-TiO$_2$, and CN/La-N-TiO$_2$ are thereby estimated to be 2.70 eV, 2.98 eV, 2.77 eV, 2.62 eV, and 2.46 eV, respectively, which is consistent with the redshift of their absorption edges.
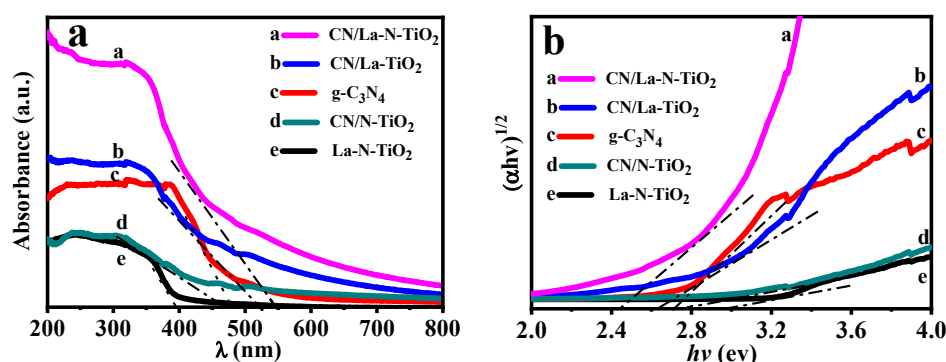
Figure 6. UV-vis spectra (**a**) of g-C$_3$N$_4$ La-N-TiO$_2$, CN/N-TiO$_2$, CN/La-TiO$_2$, and CN/La-N-TiO$_2$ composites, and (**b**) a plot of $(\alpha h\upsilon)^{1/2}$ versus the photon energy (hυ).

3.2. Photocatalytic Performance

Many studies have demonstrated that catalyst dosage, solution pH, and coexisting cations have a considerable impact on the removal efficiency of the pollutant. From an economic perspective and for designing large-scale treatment processes, the determination of optimum parameters for the removal of CIP by CN/La-N-TiO$_2$ is important. The main influential factors such as pH of the solution, initial CIP concentration, catalyst dosage, and -coexisting ions were investigated in detail and shown in Figure 7a–f.
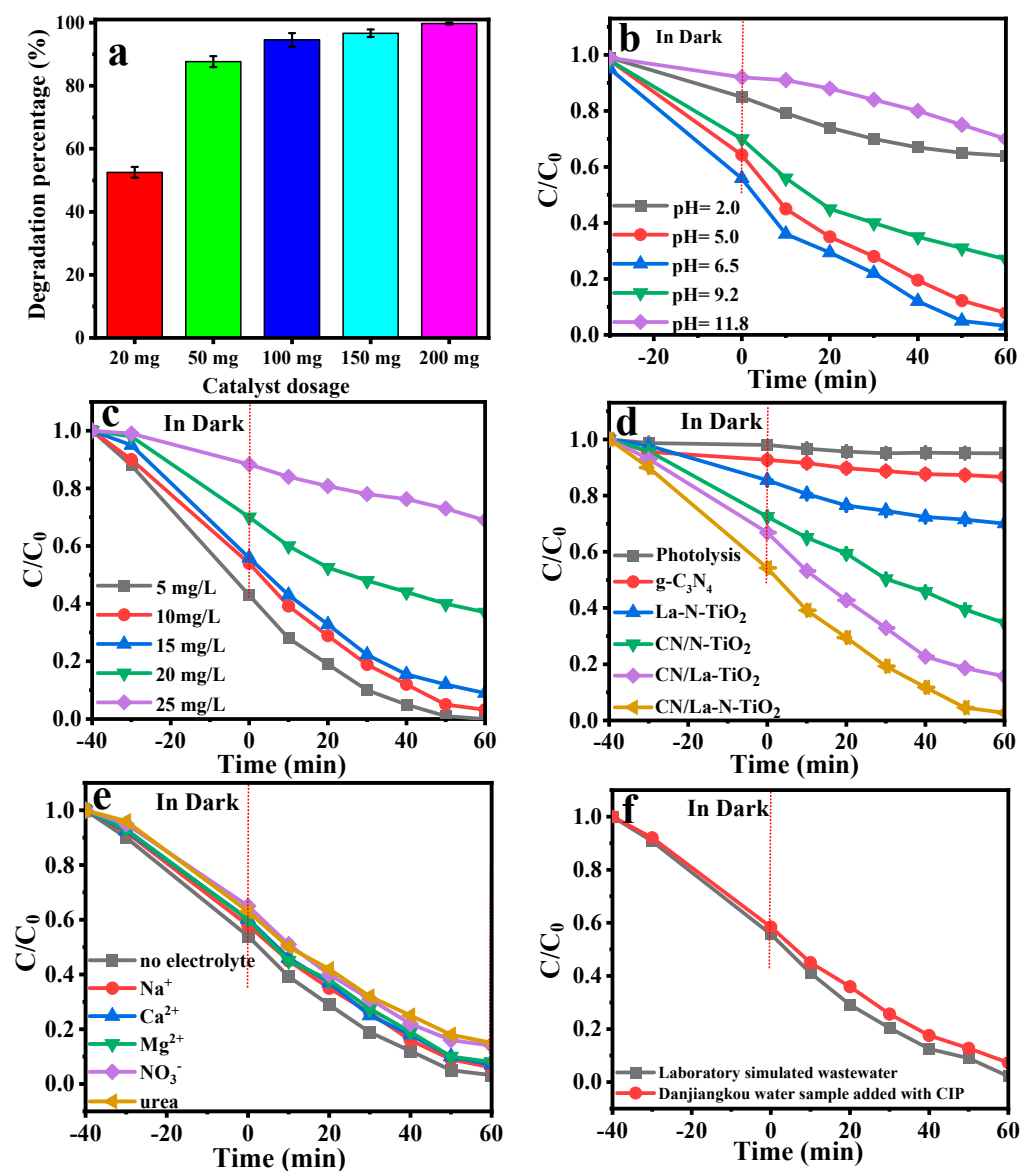
Figure 7. Photocatalytic degradation of ciprofloxacin under simulated solar- light irradiation (**a**) amount of catalyst, (**b**) at different initial pH, (**c**) Effects of the initial concentration of CIP (5–25 mg/L), (**d**) by different photocatalysts, (**e**) Effect of various electrolytes, and (**f**) in actual water samples in the presence of CN/La-N-TiO$_2$.

3.2.1. Effect of Catalyst Dosage

The effect of catalyst dosage was explored and shown in Figure 7a. When the CN/La-N-TiO$_2$ dosage increased from 0.1 g/L to 1 g/L, the removal efficiency of CIP increased from 51.5% to 96.8%. This is because the number of the active sites on the catalyst surface for radical formation increased by increasing the catalyst dosage, leading to a higher photocatalysis activity. However, when the CN/La-N-TiO$_2$ dosage was further increased above 0.75 g/L, the removal efficiency of CIP did not significantly vary. For the above-mentioned facts, 150 mg was considered the optimum dosage for the treatment of 200 mL CIP solution with a concentration of 10 mg/L.

3.2.2. Effect of pH

In Figure 8, the zeta potential values measured for CN/La-N-TiO$_2$ as a function of pH are plotted. It is observed that at pH values around 3 the zeta potential is about +24 mV,

but at pH values between 4 and 5, there is a rapid decrease of the zeta potential, the IEP occurring at pH 4.6 [59]. Hence, the catalyst surface is negatively charged at above a value of pH 4.6, while it is positively charged at below a value of pH 4.6. CIP is an amphoteric drug with a pK_a value of 6.1 (for –COOH) and 8.9 (for -NH- and -N- on the piperazinyl ring), where the isoelectric point lies at pH = 7.4 [28,60]. Therefore, CIP zwitterion will present three different ionic forms, mainly depending on the pH value of the solution. As CIP and CN/La-N-TiO$_2$ are pH sensitive, pH will influence the characteristics of both CIP and CN/La-N-TiO$_2$ as well as the interactions between them which change as pH changes.
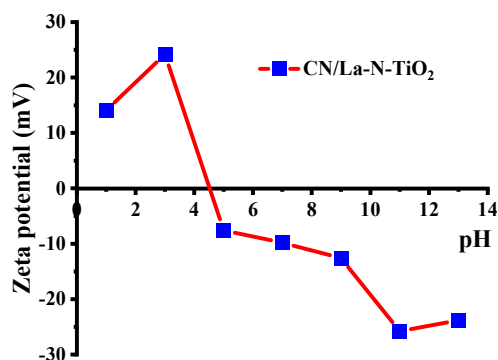
Figure 8. Zeta potential of CN/La-N-TiO$_2$ in different pH conditions.

The plots of the effect of pH (2–11.8) on CIP photodegradation with an initial concentration of 10 mg L^{-1} were studied in presence of CN/La-N-TiO$_2$ under visible light and shown in Figure 7b. The 0.05 mol·L^{-1} HCl or 0.05 mol·L^{-1} NaOH solution was used to adjust the pH value of the simulated CIP wastewater solution. It can be seen from Figure 7b, the degradation is strongly inhibited at highly acidic and basic pH and the degradation efficiency reduces from 96.8% (pH = 6.5) to 35.2% at pH = 2 and 30.5% at pH = 11.8. It is because CIP and CN/La-N-TiO$_2$ are negatively charged leading to decreased interactions at higher pH, while the generation of ·OH radicals is inhibited in an alkaline medium. It can be concluded that the optimum pH value of the CIP wastewater solution is in the pH range 6–7.

3.2.3. Effect of Initial CIP Concentrations

It can be found in Figure 7c that CIP with an initial concentration of 5 mg/L has been completely removed after 60 min of irradiation, while the relatively stable degradation efficiency is observed when the concentration increases to 10 mg/L. However, a further increase in initial CIP concentration from 10 to 20 mg/L resulted in a decrease in degradation efficiency from 96.8% to 31.2%. This is probably due to the number of surface-active sites on the catalyst provided by 150 mg CN/La-N-TiO$_2$ are not enough for a higher initial CIP concentration. Additionally, the higher the concentration, the more intermediates are generated. The generated intermediates would compete with the CIP molecules to contact the active sites on the catalyst surface, so as to inhibit the degradation of CIP.

3.2.4. Different Photocatalysts

Under the optimal conditions, where the pH value is 6.5, initial CIP concentration is 10 mg·L^{-1}, and the catalyst dosage is 0.75 g/L, the degradation experiment of CIP was carried out. As shown in Figure 7d, on a blank experiment, the self-photolysis removal of CIP was negligible. Under simulated solar- light irradiation, 15.2 %, 30.2%, 65.4%, 85.8%, and 96.8% of the CIP were degraded in 60 min by g-C$_3$N$_4$, La-N-TiO$_2$, CN/N-TiO$_2$, CN/La-TiO$_2$, and CN/La-N-TiO$_2$, respectively. CN/La-N-TiO$_2$ shows the highest CIP degradation of 96.8% in 60 min of irradiation followed by CN/La-TiO$_2$ (85.8%) and CN/N-TiO$_2$ (65.4%), indicating that the combination among La-N-co-doped TiO$_2$ and g-C$_3$N$_4$ hybrid photocatalyst can significantly enhance the photocatalytic properties.

3.2.5. Effect of Coexisting Cations

Natural water body contains various ions and organics, which would affect the photodegradation of CIP. In this work, removal of CIP by CN/La-N-TiO$_2$ was tested in presence of Na$^+$ (10 mg·L^{-1}), Ca^{2+} (10 mg·L^{-1}), Mg^{2+} (10 mg·L^{-1}), NO$_3^-$ (10 mg·L^{-1}), and urea (5 mg·L^{-1}) (Figure 7e). The concentrations of ions and urea used are representative of Danjiangkou's natural water body. It can be found in Figure 7e that Na$^+$, Ca^{2+}, and Mg^{2+} have little effect on photocatalytic activity, where NO$_3^-$ and urea obviously hindered the photocatalytic degradation of CIP.

3.2.6. Degradation in Water Sample of Dangjiangkou

In order to study the effect of the actual water application of CN/La-N-TiO$_2$. The degradation experiment of CIP in the water sample of Dangjiangkou was studied. As shown in Figure 7f, there is little reduction in degradation rate compared to laboratory simulated CIP wastewater. Therefore, CN/La-N-TiO$_2$ has a good practical application prospect.

Furthermore, the stability and reusability of CN/La-N-TiO$_2$ were evaluated via four successive cycles of CIP photocatalytic degradation experiments, where the removal rate of CIP remained almost unchanged in the cycles (Figure 9a). Meanwhile, to further explore the photocatalytic stability, the XRD patterns of CN/La-N-TiO$_2$ before and after the cycling experiment were examined (Figure 9b). It can be found that the crystallinity was almost unchanged throughout the 4 cycles. Thus, the synthesized CN/La-N-TiO$_2$ exhibits good stability and reusability, a property that is very in demand for practical applications.
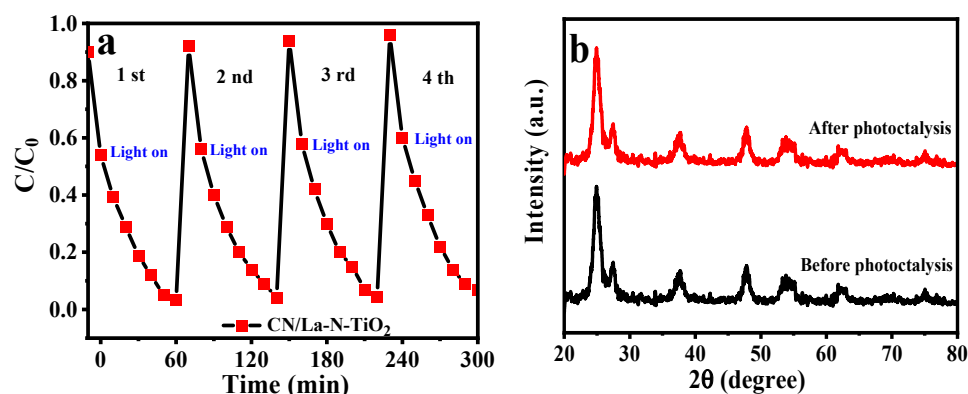
Figure 9. (**a**) Cycling experiment for the CIP removal over CN/La-N-TiO$_2$ and (**b**) XRD patterns of CN/La-N-TiO$_2$ before and after the cycling experiment.

3.2.7. Proposed Pathways of CIP Degradation

In order to estimate the toxicity of intermediates and better elucidate the mineralization pathway of CIP, the byproducts formed during the 10 min and 30 min -photocatalytic experiment were analyzed by HR-MS. According to the byproducts and a literature study [9,10,12,17,19,61], the probable degradation pathway is conceived and proposed in Figure 10. A high-intensity peak (m/z = 332) is corresponding with the original CIP molecule and the intensity of the CIP peak decreased to 20% after 10 min of degradation reaction in presence of CN/La-N-TiO$_2$ under visible light. Beyond CIP, six other -byproducts are detected including BP-1 (m/z = 362), BP-5 (m/z = 346), BP-2 (m/z = 306), BP-3 (m/z = 263), BP-4 (m/z = 246), and BP-6 (m/z = 200) (In Figure S2). It can be observed that $\cdot\cdot$O$_2^-$and h$^+$ direct attack as the main attacking species to attack the aromatic tertiary amine group, carboxyl group, and the secondary aliphatic amine group in the piperazine ring, which are three principal reactive sites in CIP in this photocatalytic system [62]. Generally, the intermediates formed showed less toxicity than the original chemical, which proved that CN/La-N-TiO$_2$ is a promising photocatalyst in the CIP wastewater treatment [10,12].

Int. J. Environ. Res. Public Health **2022**, *19*, 4793

13 of 17
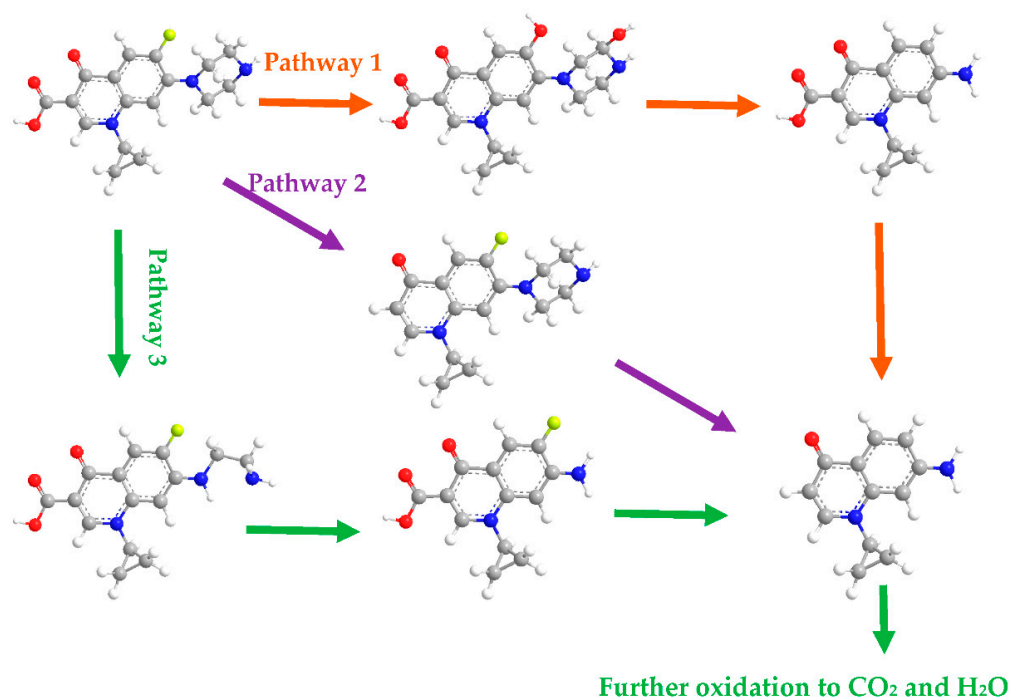
**Figure 10.** Suggested pathways for ciprofloxacin degradation in $CN/La-N-TiO_2$.

3.2.8. Radical Trapping Experiment and Possible Photocatalytic Mechanism

In order to identify the active oxidative species in the photocatalytic process, trapping experiments are carried out in the $CN/La-N-TiO_2$ hybrid photocatalytic system. Scheme 1a shows the photocatalytic degradation rate of $CN/La-N-TiO_2$ in the presence of different scavengers. The photocatalytic efficiency decreases a little by the addition of t-BuOH (TBA, ·OH scavenger, decreases to 90.5%), while it is remarkably suppressed when EDTA-2Na (h^+ scavenger decreases to 62.6%) and p-Benzoquinone (p-BQ, $·O_2^-$ decreases to 70.8%) were added to the system. Therefore, it can be inferred that the active species affect the photocatalytic activity in the following order: $h^+ > ·O_2^- > ·OH$ [32].

Based on the above results, here a possible photocatalytic mechanism of $g-C_3N_4/La-N-TiO_2$ composite was discussed and shown in Scheme 1b. The following empirical equation: $E_{VB} = \chi - E_c + 0.5E_g$ were also employed to calculate the VB and CB potentials, where χ is the electronegativity of the semiconductor. For $g-C_3N_4$ and TiO_2, χ is 4.73 and 5.81, respectively [42,45]. E_c is the energy of free electrons based on the hydrogen scale (4.50 eV). The E_{VB} and E_{CB} edge potentials of $La-N-TiO_2$ were calculated to be +2.80 eV and −0.18 eV, respectively, and those of $g-C_3N_4$ were +1.55 eV and −1.25 eV, respectively.
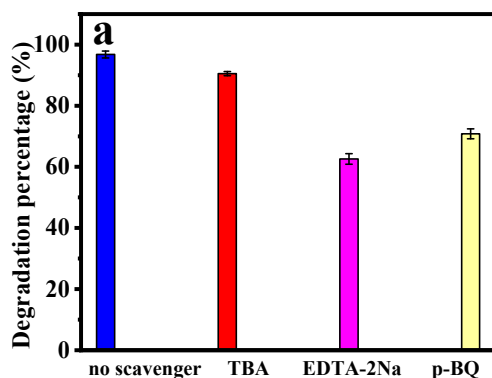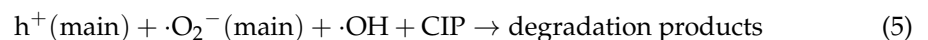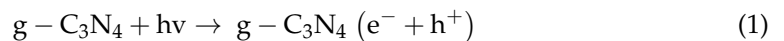

Scheme 1. *Cont.*
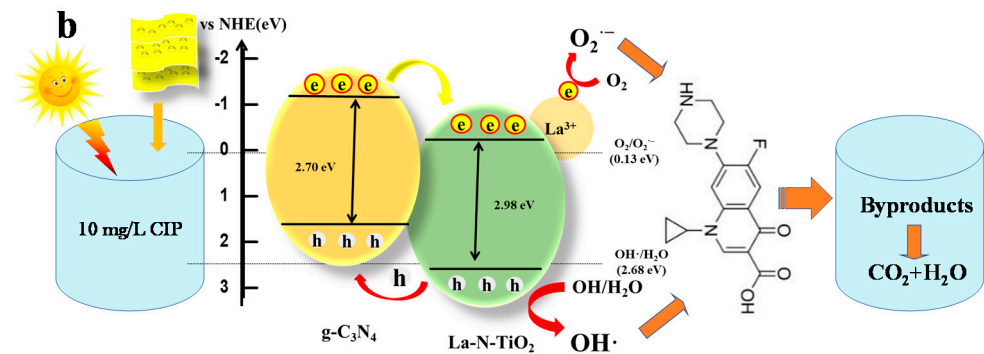
Scheme 1. (**a**) Photocatalytic activity of CN/La-N-TiO$_2$ toward CIP degradation in the presence of different scavengers and (**b**) schematic diagram for photocatalytic removal CIP mechanism by CN/La-N-TiO$_2$ photocatalyst under simulated solar light irradiation.

Under simulated solar light illumination, both g-C$_3$N$_4$ and La-N-TiO$_2$ could be stimulated and generate electron-hole (e$^-$-h$^+$) pairs [42,45]. Due to the CB potential of g-C$_3$N$_4$ (−1.25 eV) being lower than that of La-N-TiO$_2$ (−0.18 eV), the photo-induced electrons would shift from the CB of g-C$_3$N$_4$ to the CB of g-C$_3$N$_4$ through the heterointerface. The e$^-$ generated in g-C$_3$N$_4$ goes to TiO$_2$, where La^{3+} with 4f orbit can easily capture O$_2$ adsorbed on the surface of TiO$_2$ to form superoxide anion (·O$_2$$^-$) [23,41,45,56].

Part of the holes (h$^+$) in the VB of TiO$_2$ can easily be transferred to the VB of g-C$_3$N$_4$. Due to the lower reduction potential of the VB of g-C$_3$N$_4$ (1.55 eV vs. NHE), h$^+$ in the VB of g-C$_3$N$_4$ can be used to degrade CIP directly. The remaining h$^+$ at the VB potential of La-N-TiO$_2$ (2.80 V vs. NHE) can oxidize water into hydroxyl radicals (·OH), owing to their potential being higher than the H$_2$O/·OH potential (2.68 eV vs. NHE) [42]. Thus, during the photocatalytic reaction, h + and ·O$_2$$^-$ are the most important active species.

$$g - C_3N_4 + hv \rightarrow g - C_3N_4 \left(e^- + h^+\right) \tag{1}$$

$$La - N - TiO_2 + hv \rightarrow La - N - TiO_2 \left(e^- + h^+\right) \tag{2}$$

$$h^+ + H_2O \rightarrow \cdot OH \tag{3}$$

$$La^{3+} + e^- + O_2 \rightarrow \cdot O_2^- \tag{4}$$

$$h^+(main) + \cdot O_2^-(main) + \cdot OH + CIP \rightarrow degradation \ products \tag{5}$$

4. Conclusions

A 3D nanocomposite photocatalyst g-C$_3$N$_4$/La-N-TiO$_2$ was successfully synthesized by a simple and reproducible in-situ synthetic method. g-C$_3$N$_4$/La-N-TiO$_2$ exhibits high photocatalytic activity for the degradation of ciprofloxacin. A 96.8% degradation of CIP was achieved in 60 min under the conditions of 0.75 g·L^{-1} CN/La-N-TiO$_2$, 10 mg·L^{-1} CIP, and pH of 6.5. The excellent photocatalytic performance of CN/La-N-TiO$_2$ on degrading CIF is attributed to the formation of a junction that efficiently improves charge separation and wide spectrum response. The removal rates were rarely affected by Na$^+$ (10 mg·L^{-1}), Ca^{2+} (10 mg·L^{-1}), Mg^{2+} (10 mg·L^{-1}), and urea (5 mg·L^{-1}), where the concentrations of ions and urea used are representative of Danjiangkou natural water body. In addition, the intermediates formed showed less toxicity than the original chemical, which proved that CN/La-N-TiO$_2$ nanocomposite is a green and promising photocatalyst for large-scale applications and would be a candidate for the removal of the emerging antibiotics present in the water environment.

References

1. Sarmah, A.K.; Meyer, M.T.; Boxall, A.B. A global perspective on the use, sales, exposure pathways, occurrence, fate and effects of veterinary antibiotics (VAs) in the environment. *Chemosphere* **2006**, *65*, 725–759. [CrossRef] [PubMed]

2. Liu, Y.Y.; Wang, Y.; Walsh, T.R.; Yi, L.X.; Zhang, R.; Spencer, J.; Doi, Y.; Tian, G.; Dong, B.; Huang, X.; et al. Emergence of plasmid-mediated colistin resistance mechanism MCR-1 in animals and human beings in China: A microbiological and molecular biological study. *Lancet Infect. Dis.* **2016**, *16*, 161–168. [CrossRef]

3. Qiao, M.; Ying, G.G.; Singer, A.C.; Zhu, Y.G. Review of antibiotic resistance in China and its environment. *Environ. Int.* **2018**, *110*, 160–172. [CrossRef] [PubMed]

4. Chen, Y.; Yang, J.; Zeng, L.; Zhu, M. Recent progress on the removal of antibiotic pollutants using photocatalytic oxidation process. *Crit. Rev. Environ. Sci. Technol.* **2021**, *52*, 1401–1448. [CrossRef]

5. Boger, B.; Surek, M.; Vilhena, R.O.; Fachi, M.M.; Junkert, A.M.; Santos, J.M.; Domingos, E.L.; Cobre, A.F.; Momade, D.R.; Pontarolo, R. Occurrence of antibiotics and antibiotic resistant bacteria in subtropical urban rivers in Brazil. *J. Hazard. Mater.* **2020**, *402*, 123448. [CrossRef]

6. Feng, M.; Wang, Z.; Dionysiou, D.D.; Sharma, V.K. Metal-mediated oxidation of fluoroquinolone antibiotics in water: A review on kinetics, transformation products, and toxicity assessment. *J. Hazard. Mater.* **2018**, *344*, 1136–1154. [CrossRef]

7. Qian, Q.Z.; Guang, G.Y.; Chang, G.P.; You, S.L.; Jian, L.Z. Comprehensive evaluation of antibiotics emission and fate in the river basins of china: Source analysis, multimedia modeling, and linkage to bacterial resistance. *Environ. Sci. Technol.* **2015**, *49*, 6772–6782.

8. Huang, F.; An, Z.; Moran, M.J.; Liu, F. Recognition of typical antibiotic residues in environmental media related to groundwater in China (2009–2019). *J. Hazard. Mater.* **2020**, *399*, 122813. [CrossRef]

9. An, T.; Yang, H.; Li, G.; Song, W.; Cooper, W.J.; Nie, X. Kinetics and mechanism of advanced oxidation processes (AOPs) in degradation of ciprofloxacin in water. *Appl. Catal. B Environ.* **2010**, *94*, 288–294. [CrossRef]

10. Liu, H.; Gao, Y.; Wang, J.; Ma, D.; Wang, Y.; Gao, B.; Yue, Q.; Xu, X. The application of UV/O$_3$ process on ciprofloxacin wastewater containing high salinity: Performance and its degradation mechanism. *Chemosphere* **2021**, *276*, 130220. [CrossRef]

11. Rakshit, S.; Sarkar, D.; Elzinga, E.J.; Punamiya, P.; Datta, R. Mechanisms of ciprofloxacin removal by nano-sized magnetite. *J. Hazard. Mater.* **2013**, *246*, 221–226. [CrossRef] [PubMed]

12. Cai, Y.; Yan, Z.; Ou, Y.; Peng, B.; Zhang, L.; Shao, J.; Lin, Y.; Zhang, J. Effects of different carbon sources on the removal of ciprofloxacin and pollutants by activated sludge: Mechanism and biodegradation. *J. Environ. Sci.* **2022**, *111*, 240–248. [CrossRef] [PubMed]

13. Ma, Y.; Li, M.; Wu, M.; Li, Z.; Liu, X. Occurrences and regional distributions of 20 antibiotics in water bodies during groundwater recharge. *Sci. Total Environ.* **2015**, *518*, 498–506. [CrossRef] [PubMed]

14. Jiang, W.T.; Chang, P.H.; Wang, Y.S.; Tsai, Y.; Jean, J.S.; Li, Z.; Krukowski, K. Removal of ciprofloxacin from water by birnessite. *J. Hazard. Mater.* **2013**, *250*, 362–369. [CrossRef]

15. Tang, J.; Shi, T.; Wu, X.; Cao, H.; Li, X.; Hua, R.; Tang, F.; Yue, Y. The occurrence and distribution of antibiotics in Lake Chaohu, China: Seasonal variation, potential source and risk assessment. *Chemosphere* **2015**, *122*, 154–161. [CrossRef]

16. Zhang, X.; Li, R.; Jia, M.; Wang, S.; Huang, Y.; Chen, C. Degradation of ciprofloxacin in aqueous bismuth oxybromide (BiOBr) suspensions under visible light irradiation: A direct hole oxidation pathway. *Chem. Eng. J.* **2015**, *274*, 290–297. [CrossRef]

17. Li, Y.; Han, J.; Xie, B.; Li, Y.; Zhan, S.; Tian, Y. Synergistic degradation of antimicrobial agent ciprofloxacin in water by using 3D CeO$_2$/RGO composite as cathode in electro-Fenton system. *J. Electroanal. Chem.* **2017**, *784*, 6–12. [CrossRef]

18. Egbedina, A.O.; Adebowale, K.O.; Olu-Owolabi, B.I.; Unuabonah, E.I.; Adesina, M.O. Green synthesis of ZnO coated hybrid biochar for the synchronous removal of ciprofloxacin and tetracycline in wastewater. *RSC Adv.* **2021**, *11*, 18483–18492. [CrossRef]

19. Paul, T.; Dodd, M.C.; Strathmann, T.J. Photolytic and photocatalytic decomposition of aqueous ciprofloxacin: Transformation products and residual antibacterial activity. *Water Res.* **2010**, *44*, 3121–3132. [CrossRef]

20. Di, J.; Xia, J.; Ji, M.; Yin, S.; Li, H.; Xu, H.; Zhang, Q.; Li, H. Controllable synthesis of $Bi_4O_5Br_2$ ultrathin nanosheets for photocatalytic removal of ciprofloxacin and mechanism insight. *J. Mater. Chem. A* **2015**, *3*, 15108–15118. [CrossRef]

21. Chen, M.; Chu, W. H_2O_2 assisted degradation of antibiotic norfloxacin over simulated solar light mediated Bi_2WO_6: Kinetics and reaction pathway. *Chem. Eng. J.* **2016**, *296*, 310–318. [CrossRef]

22. Ding, Q.; Lam, F.L.Y.; Hu, X. Complete degradation of ciprofloxacin over g-C_3N_4-iron oxide composite via heterogeneous dark Fenton reaction. *J. Environ. Manage.* **2019**, *244*, 23–32. [CrossRef]

23. Zhang, H.; Li, W.; Yan, Y.; Wang, W.; Ren, Y.; Li, X. Synthesis of highly porous g-C_3N_4 nanotubes for efficient photocatalytic degradation of sulfamethoxazole. *Mater. Today Commun.* **2021**, *27*, 102288. [CrossRef]

24. Gad-Allah, T.A.; Ali, M.E.; Badawy, M.I. Photocatalytic oxidation of ciprofloxacin under simulated sunlight. *J. Hazard. Mater.* **2011**, *186*, 751–755. [CrossRef] [PubMed]

25. Wen, X.J.; Niu, C.G.; Zhang, L.; Liang, C.; Guo, H.; Zeng, G.M. Photocatalytic degradation of ciprofloxacin by a novel Z-scheme CeO_2–Ag/AgBr photocatalyst: Influencing factors, possible degradation pathways, and mechanism insight. *J. Catal.* **2018**, *358*, 141–154. [CrossRef]

26. Rahmani-Aliabadi, A.; Nezamzadeh-Ejhieh, A. A visible light FeS/Fe_2S_3/zeolite photocatalyst towards photodegradation of ciprofloxacin. *J. Photochem. Photobiol. A Chem.* **2018**, *357*, 1–10. [CrossRef]

27. Gan, Y.; Wei, Y.; Xiong, J.; Cheng, G. Impact of post-processing modes of precursor on adsorption and photocatalytic capability of mesoporous TiO_2 nanocrystallite aggregates towards ciprofloxacin removal. *Chem. Eng. J.* **2018**, *349*, 1–16. [CrossRef]

28. El-Kemary, M.; El-Shamy, H.; El-Mehasseb, I. Photocatalytic degradation of ciprofloxacin drug in water using ZnO nanoparticles. *J. Lumin.* **2010**, *130*, 2327–2331. [CrossRef]

29. Li, N.; Zhang, J.; Tian, Y.; Zhao, J.; Zhang, J.; Zuo, W. Precisely controlled fabrication of magnetic 3D γ-Fe_2O_3@ZnO core-shell photocatalyst with enhanced activity: Ciprofloxacin degradation and mechanism insight. *Chem. Eng. J.* **2017**, *308*, 377–385. [CrossRef]

30. Chen, M.; Yao, J.; Huang, Y.; Gong, H.; Chu, W. Enhanced photocatalytic degradation of ciprofloxacin over $Bi_2O_3/(BiO)_2CO_3$ heterojunctions: Efficiency, kinetics, pathways, mechanisms and toxicity evaluation. *Chem. Eng. J.* **2018**, *334*, 453–461. [CrossRef]

31. Deng, Y.; Tang, L.; Feng, C.; Zeng, G.; Wang, J.; Zhou, Y.; Liu, Y.; Peng, B.; Feng, H. Construction of plasmonic Ag modified phosphorous-doped ultrathin g-C_3N_4 nanosheets/$BiVO_4$ photocatalyst with enhanced visible-near-infrared response ability for ciprofloxacin degradation. *J. Hazard. Mater.* **2018**, *344*, 758–769. [CrossRef] [PubMed]

32. Guo, N.; Zeng, Y.; Li, H.; Xu, X.; Yu, H.; Han, X. Novel mesoporous TiO_2@g-C_3N_4 hollow core@shell heterojunction with enhanced photocatalytic activity for water treatment and H_2 production under simulated sunlight. *J. Hazard. Mater.* **2018**, *353*, 80–88. [CrossRef] [PubMed]

33. Kumar, A.; Sharma, G.; Naushad, M.; Ahamad, T.; Veses, R.C.; Stadler, F.J. Highly visible active Ag_2CrO_4/Ag/$BiFeO_3$@RGO nano-junction for photoreduction of CO_2 and photocatalytic removal of ciprofloxacin and bromate ions: The triggering effect of Ag and RGO. *Chem. Eng. J.* **2019**, *370*, 148–165. [CrossRef]

34. Hu, K.; Li, R.; Ye, C.; Wang, A.; Wei, W.; Hu, D.; Qiu, R.; Yan, K. Facile synthesis of Z-scheme composite of TiO_2 nanorod/g-C_3N_4 nanosheet efficient for photocatalytic degradation of ciprofloxacin. *J. Clean. Prod.* **2020**, *253*, 120055. [CrossRef]

35. Gandamalla, A.; Manchala, S.; Verma, A.; Fu, Y.P.; Shanker, V. Microwave-assisted synthesis of ZnAl-LDH/g-C_3N_4 composite for degradation of antibiotic ciprofloxacin under visible-light illumination. *Chemosphere* **2021**, *283*, 131182. [CrossRef]

36. Liu, X.; Lv, P.; Yao, G.; Ma, C.; Tang, Y.; Wu, Y.; Huo, P.; Pan, J.; Shi, W.; Yan, Y. Selective degradation of ciprofloxacin with modified NaCl/TiO_2 photocatalyst by surface molecular imprinted technology. *Colloids Surf. A Physicochem. Eng. Asp.* **2014**, *441*, 420–426. [CrossRef]

37. Rong, X.; Qiu, F.; Jiang, Z.; Rong, J.; Pan, J.; Zhang, T.; Yang, D. Preparation of ternary combined ZnO-Ag_2O/porous g-C_3N_4 composite photocatalyst and enhanced visible-light photocatalytic activity for degradation of ciprofloxacin. *Chem. Eng. Res. Des.* **2016**, *111*, 253–261. [CrossRef]

38. Kumar, A.; Kumar, A.; Sharma, G.; Naushad, M.; Veses, R.C.; Ghfar, A.A.; Stadler, F.J.; Khan, M.R. Solar-driven photodegradation of 17-β-estradiol and ciprofloxacin from waste water and CO_2 conversion using sustainable coal-char/polymeric-g-C_3N_4/RGO metal-free nano-hybrids. *New J. Chem.* **2017**, *41*, 10208–10224. [CrossRef]

39. Feng, X.; Wang, P.; Hou, J.; Qian, J.; Ao, Y.; Wang, C. Significantly enhanced visible light photocatalytic efficiency of phosphorus doped TiO_2 with surface oxygen vacancies for ciprofloxacin degradation: Synergistic effect and intermediates analysis. *J. Hazard. Mater.* **2018**, *351*, 196–205. [CrossRef]

40. Li, C.; Sun, Z.; Zhang, W.; Yu, C.; Zheng, S. Highly efficient g-C_3N_4/TiO_2/kaolinite composite with novel three-dimensional structure and enhanced visible light responding ability towards ciprofloxacin and S. aureus. *Appl. Catal. B Environ.* **2018**, *220*, 272–282. [CrossRef]

41. Kuila, S.K.; Gorai, D.K.; Gupta, B.; Gupta, A.K.; Tiwary, C.S.; Kundu, T.K. Lanthanum ions decorated 2-dimensional g-C_3N_4 for ciprofloxacin photodegradation. *Chemosphere* **2021**, *268*, 128780. [CrossRef] [PubMed]

42. Yu, Y.; Geng, J.; Li, H.; Bao, R.; Chen, H.; Wang, W.; Xia, J.; Wong, W. Exceedingly high photocatalytic activity of g-C_3N_4/Gd-N-TiO_2 composite with nanoscale heterojunctions. *Sol. Energy Mater. Sol. Cells* **2017**, *168*, 91–99. [CrossRef]

Int. J. Environ. Res. Public Health **2022**, *19*, 4793

17 of 17

43. Yu, Y.; Xia, J.; Chen, C.; Chen, H.; Geng, J.; Li, H. One-step synthesis of a visible-light driven C@N-TiO$_2$ porous nanocomposite: Enhanced absorption, photocatalytic and photoelectrochemical performance. *J. Phys. Chem. Solids* **2020**, *136*, 109169. [CrossRef]

44. Bao, R.; Yu, Y.; Chen, H.; Wang, W.; Xia, J.; Li, H. Effects of Rare Earth Elements and Nitrogen Co-Doped on the Photocatalytic Performance of TiO$_2$. *Cryst. Res. Technol.* **2018**, *53*, 1700138. [CrossRef]

45. Li, J.; Du, L.; Jia, S.; Sui, G.; Zhang, Y.; Zhuang, Y.; Li, B.; Xing, Z. Synthesis and photocatalytic properties of visible-light-responsive, three-dimensional, flower-like La–TiO$_2$/g-C$_3$N$_4$ heterojunction composites. *RSC Adv.* **2018**, *8*, 29645–29653. [CrossRef]

46. Meksi, M.; Turki, A.; Kochkar, H.; Bousselmi, L.; Guillard, C.; Berhault, G. The role of lanthanum in the enhancement of photocatalytic properties of TiO$_2$ nanomaterials obtained by calcination of hydrogenotitanate nanotubes. *Appl. Catal. B Environ.* **2016**, *181*, 651–660. [CrossRef]

47. Yu, Y.; Piao, L.; Xia, J.; Wang, W.; Geng, J.; Chen, H.; Xing, X.; Li, H. A facile one-pot synthesis of N-La codoped TiO$_2$ porous materials with bio-hierarchical architectures and enhanced photocatalytic activity. *Mater. Chem. Phys.* **2016**, *182*, 77–85. [CrossRef]

48. Raaja Rajeshwari, M.; Kokilavani, S.; Sudheer Khan, S. Recent developments in architecturing the g-C$_3$N$_4$ based nanostructured photocatalysts: Synthesis, modifications and applications in water treatment. *Chemosphere* **2021**, *291*, 132735. [CrossRef]

49. Deng, H.; Wang, X.C.; Wang, L.; Lia, Z.J.; Liang, P.L.; Ou, J.Z.; Liu, K.; Yuan, L.Y.; Jiang, Z.Y.; Zheng, L.R.; et al. Enhanced photocatalytic reduction of aqueous Re (VII) in ambient air by amorphous TiO$_2$/g-C$_3$N$_4$ photocatalysts: Implications for Tc (VII) elimination. *Chem. Eng. J.* **2020**, *401*, 125977. [CrossRef]

50. Liu, G.; Niu, P.; Sun, C.; Smith, S.C.; Chen, Z.; Lu, G.; Cheng, H. Unique Electronic Structure Induced High Photoreactivity of Sulfur-Doped Graphitic C$_3$N$_4$. *J. Am. Chem. Soc.* **2010**, *132*, 11642–11648. [CrossRef]

51. Ahmaruzzaman, M.; Mishra, S.R. Photocatalytic performance of g-C$_3$N$_4$ based nanocomposites for effective degradation/removal of dyes from water and wastewater. *Mater. Res. Bull.* **2021**, *143*, 111417. [CrossRef]

52. Sun, C.; Dai, J.; Zhang, H.; Li, S.; Wang, A. A facile method for preparing porous g-C$_3$N$_4$ nanosheets with efficient photocatalytic activity under visible light. *J. Mater. Sci.* **2021**, *56*, 7557–7572. [CrossRef]

53. Hao, D.; Huang, Q.; Wei, W.; Bai, X.; Ni, B.J. A reusable, separation-free and biodegradable calcium alginate/g-C$_3$N$_4$ microsphere for sustainable photocatalytic wastewater treatment. *J. Clean. Prod.* **2021**, *314*, 128033. [CrossRef]

54. Hu, H.; Hu, J.; Wang, X.; Gan, J.; Su, M.; Ye, W.; Zhang, W.; Ma, X.; Wang, H. Enhanced reduction and oxidation capability over the CeO$_2$/g-C$_3$N$_4$ hybrid through surface carboxylation: Performance and mechanism. *Catal. Sci. Technol.* **2020**, *10*, 4712–4725. [CrossRef]

55. Karuppaiah, M.; Benadict Joseph, X.; Wang, S.F.; Sriram, B.; Antilen Jacob, G.; Ravi, G. Engineering Architecture of 3D-Urchin-like Structure and 2D-Nanosheets of Bi$_2$S$_3$@g-C$_3$N$_4$ as the Electrode Material for a Solid-State Symmetric Supercapacitor. *Energy Fuels* **2021**, *35*, 12569–12580. [CrossRef]

56. Li, Y.; Wang, J.; Yang, Y.; Zhang, Y.; He, D.; An, Q.; Cao, G. Seed-induced growing various TiO$_2$ nanostructures on g-C$_3$N$_4$ nanosheets with much enhanced photocatalytic activity under visible light. *J. Hazard. Mater.* **2015**, *292*, 79–89. [CrossRef]

57. Chen, Y.; Wu, Q.; Wang, J.; Song, Y. Visible-light-driven elimination of oxytetracycline and Escherichia coli using magnetic La-doped TiO$_2$/copper ferrite/diatomite composite. *Environ. Sci. Pollut. Res.* **2019**, *26*, 26593–26604. [CrossRef]

58. Makula, P.; Pacia, M.; Macyk, W. How To Correctly Determine the Band Gap Energy of Modified Semiconductor Photocatalysts Based on UV-Vis Spectra. *J. Phys. Chem. Lett.* **2018**, *9*, 6814–6817. [CrossRef]

59. Fazio, S.; Guzmán, J.; Colomer, M.T.; Salomoni, A.; Moreno, R. Colloidal stability of nanosized titania aqueous suspensions. *J. Eur. Ceram. Soc.* **2008**, *28*, 2171–2176. [CrossRef]

60. Salma, A.; Thoroe-Boveleth, S.; Schmidt, T.C.; Tuerk, J. Dependence of transformation product formation on pH during photolytic and photocatalytic degradation of ciprofloxacin. *J. Hazard. Mater.* **2016**, *313*, 49–59. [CrossRef]

61. Iqbal, J.; Shah, N.S.; Sayed, M. Exploring the potential of nano-zerovalent copper modified biochar for the removal of ciprofloxacin from water. Environmental Nanotechnology. *Monit. Manag.* **2021**, *16*, 100604.

62. Leng, L.; Wei, L.; Xiong, Q.; Xu, S.; Li, W.; Lv, S.; Lu, Q.; Wan, L.; Wen, Z.; Zhou, W. Use of microalgae-based technology for the removal of antibiotics from wastewater: A review. *Chemosphere* **2020**, *238*, 124680. [CrossRef] [PubMed]